A Numerical Comparative Study of the Effect of Working Fluids and Wick Properties on the Performance of Capillary Pumped Loop with a Flat Evaporator

Riadh Boubaker, Vincent Platel, Souad Harmand

Applied Thermal Engineering 100 (2016) 564–576

A numerical comparative study of the effect of working fluids and wick properties on the performance of capillary pumped loop with a flat evaporator

Riadh Boubaker [a,*], Vincent Platel [a], Souad Harmand [b]

[a] Laboratoire de Thermique, Energétique et Procédés (LaTEP), Université de Pau et des Pays de l'Adour, Rue Jules Ferry, BP 7511, 64075 Pau, France
[b] Laboratoire de LAMIH, Valenciennes, France

HIGHLIGHTS

- A complete dynamic model of a capillary pumped loop is presented.
- The heat and mass transfer inside the porous wick is described by a 2D mathematical model.
- Effects of the thermophysical properties of working fluids are extensively analyzed.
- Effects of the porous wick properties on the CPL performance are investigated.

Keywords:
Capillary pumped loop
Working fluid
Porous wick

ABSTRACT

This study presents a numerical analysis of a capillary pumped loop (CPL) performance using different working fluids and porous wick properties. A complete CPL model is used, which describes the growth of the vapor pocket inside the porous wick. The CPL behavior is studied for different working liquids, such as methanol, acetone and ethanol. Results show that methanol is the most efficient fluid in terms of thermal conductance and heat transport capacity. The present work allows also to evaluate the importance of the wick properties in the improvement of the thermal characteristics for capillary pumped loop.

1. Introduction

The increase in the thermal loads dissipated by the electronic components in the terrestrial applications requires the use of efficient heat transfer devices. Capillary pumped loops (CPL) are well known by their ability to transport large heat loads over long distances without the need of any mechanical pump [1–3].

A little effort in literature has been devoted to describe the impact of the working fluid and wick properties on the CPL performance. There are two main types of approaches aiming to study the CPL operation: the approach where the whole CPL behavior is described; however, it was assumed that the porous wick is fully saturated with liquid even for high heat loads [4–6]; and the approach where only one of the CPL components is studied. The CPL evaporator is the most studied component to investigate the heat and mass transfer with phase change inside the porous wick [7–11]. Figus et al. [7] presented two 2D steady approaches to study the heat transfer inside the porous wick: continuum model (Darcy model) and pore scale model. Both models demonstrated the existence of a vapor zone under the fins. The 2D simulation results are validated by the experimental investigations of Coquard [12]. The visualization experiments on a two-dimensional porous wick confirmed the existence of a stable vapor pocket underneath the heated surface. Later on, Mottet et al. [13] continued working on the same topic by developing a steady 3D model to describe the heat and mass transfers inside the porous wick. It was demonstrated that, for a moderate heat flux between 3.7 W/cm^2 and 7.8 W/cm^2, the phase distribution within the wick is characterized by the coexistence of both the liquid and vapor phases underneath the casing. This regime is shown to correspond to the best evaporator performance. For higher heat fluxes, a vapor pocket is formed, which is in contact with the casing.

The Capillary Pumped Loop studied in this paper can support very high thermal loads that could exceed 100 W/cm^2. By consequence, in accordance with the work of Mottet et al. [13], the vapor pocket assumption is valid for higher heat fluxes. Recently, Boubaker and Platel [14] presented a transient model of the whole CPL where it supposes the existence of vapor pocket inside the porous wick. The main originality of the proposed model consists in the combination of mass, energy and momentum equations for each

* Corresponding author. Tel.: +33 622094126; fax: +33 0562566010.
E-mail address: boubaker.riadh@gmail.com (R. Boubaker).

DOI : 10.1016/j.applthermaleng.2016.02.034

component of the system with a precise description of the complex phase change phenomena inside the porous wick. The vapor pocket behavior inside the porous wick is analyzed during CPL operation. Results show a stabilization of the vapor pocket due to the effect of the couplings of the thermal and hydrodynamic mechanisms involved in the interactions between the evaporator and the rest of the loop. The current study presents a continuation of previous work where we focus on the impact of the working fluid and the wick properties on the CPL performance.

The effect of the thermo-physical properties of the working fluids and the porous wick properties is of paramount importance on the thermal performance of heat transfer devices. Han et al. [15] studied the impact of working fluids and their properties on the performance of pulsating heat pipes. This study investigated the oscillation characteristics and the heat transfer performance of a closed-loop PHP charged with deionized water, methanol, ethanol and acetone. Bazzo and Riehl [16] conducted an experimental investigation of a small-scale CPL. The experimental tests were carried out with acetone and anhydrous ammonia as working fluids in order to analyze the CPL start-up. The results showed that anhydrous ammonia system presents a better heat transport capability compared to acetone. Liu et al. [17] investigated the impact of different working fluids on the operational characteristics of miniature LHP with flat evaporator. The difference between methanol and acetone as working fluid is especially studied in this work. Experimental results showed that the LHP–acetone start up is faster than the LHP–methanol and its evaporator wall temperature is lower at steady state. Singh et al. [18] studied the effect of wick characteristics on the thermal performance of the Miniature Loop Heat Pipe. Different materials and porous structures have been investigated to improve the efficiency of the heat exchange process inside the evaporation zone. Santos et al. [19,20] tested two LHPs with ceramic porous wick, using acetone and water as working fluids for power inputs up to 25 W. He demonstrated that the ceramic wick could be an alternative to metal and polymer for applications in LHPs and CPLs.

This study reports on a numerical investigation of the coupled effects of working fluids and the porous wick properties (conductivity and porosity) on the performance of a capillary pumped loop. To achieve this aim, a detailed CPL model is considered that takes into account the existence of a vapor pocket inside the porous wick.

2. Model description

2.1. CPL description

As shown in Fig. 1, CPL consists of an evaporator, a vapor line, a condenser, a liquid line and a reservoir. The various parameters of the CPL are listed in Table 1. The lines, reservoir, condenser and evaporator housing sides are made of stainless steel, whereas the evaporator wick and heated faces are made of nickel.

2.2. Evaporator

The evaporator is the key component of a CPL system (Fig. 2). The mathematical model was previously explained in the work of Boubaker et al. [11], where the heat and mass transfer equations are developed for a part of the wick centered around the heating element (Fig. 3). The mathematical model is based on the volume-averaged technique. Heat, momentum and mass balances are applied to a Representative Elementary Volume (REV) of the porous wick. This volume contains liquid and vapor phases of methanol and a solid phase representing the porous wick.

The dynamic growth of the vapor pocket inside the porous wick is described by the following equations:

– Continuum equation
Liquid phase

$$\frac{\partial(\rho_\ell \alpha_\ell)}{\partial t} + div\left(\rho_\ell \vec{V}_\ell\right) = -\dot{\Gamma} \tag{1}$$

Vapor phase

$$\frac{\partial(\rho_v \alpha_v)}{\partial t} + div\left(\rho_v \vec{V}_v\right) = \dot{\Gamma} \tag{2}$$

– Darcy equation
Liquid phase

$$\vec{V}_\ell = -\frac{\kappa \kappa_{r\ell}}{\mu_\ell}\vec{\nabla} p_\ell \tag{3}$$

Vapor phase

$$\vec{V}_v = -\frac{\kappa \kappa_{rv}}{\mu_v}\vec{\nabla} p_v \tag{4}$$

– Energy equation

$$\overline{\rho C}_p \frac{\partial T}{\partial t} + \left(\rho_\ell C_{p\ell}\vec{V}_\ell + \rho_v C_{pv}\vec{V}_v\right)\cdot\vec{\nabla}T = \lambda_{\text{eff}}\Delta T - \dot{\Gamma} L_v \tag{5}$$

where $\overline{\rho C}_p$ is the density–capacity heat product and λ_{eff} is the effective thermal conductivity. The determination of the effective thermal conductivity is not trivial. Many different correlations can be found in the literature to determine the effective thermal conductivity of a porous medium. In the Section 3.3, the effect of λ_{eff} on the casing temperature is investigated. In our calculations, the effective thermal conductivity is determined by a parallel model $\lambda_{\text{eff}} = (1-\varepsilon)\lambda_s + \varepsilon(\alpha_\ell \lambda_\ell + \alpha_v \lambda_v)$, which is used in several previous works [7,8,10,21–25].

– Energy equation in the casing

$$\rho_{C_E} C_{pC_E} \frac{\partial T_{C_E}}{\partial t} = \lambda_{C_E} \Delta T_{C_E} \tag{6}$$

– Phase change model

$$\dot{\Gamma} = a S_w \sqrt{\frac{M}{2\pi RT}}\left(p_{sat}(T) - p_v\right) \tag{7}$$

2.3. Condenser

The condenser model is inspired by the work of Pouzet et al. [4]. The major assumptions are:

- there is no superheated vapor zone at the condenser inlet;
- the liquid and vapor phases are incompressible [26–28];
- the vapor void fraction α_C is constant;
- the heat sink temperature and the external heat coefficient are considered uniform along the condenser.

The condenser is composed of two areas : a two-phase zone followed by a zone of sub-cooled liquid (see Fig. 4).

– Two-phase zoneThe two-phase zone is characterized by the variable length η. The viscous pressure losses in this region are neglected compared to the gravitational losses and the viscous pressure losses in the liquid line. The mass and the energy balances in this zone are given by:

$$\rho_m A_C \frac{d\eta}{dt} = \dot{m}_C - \dot{m}_v \tag{8}$$

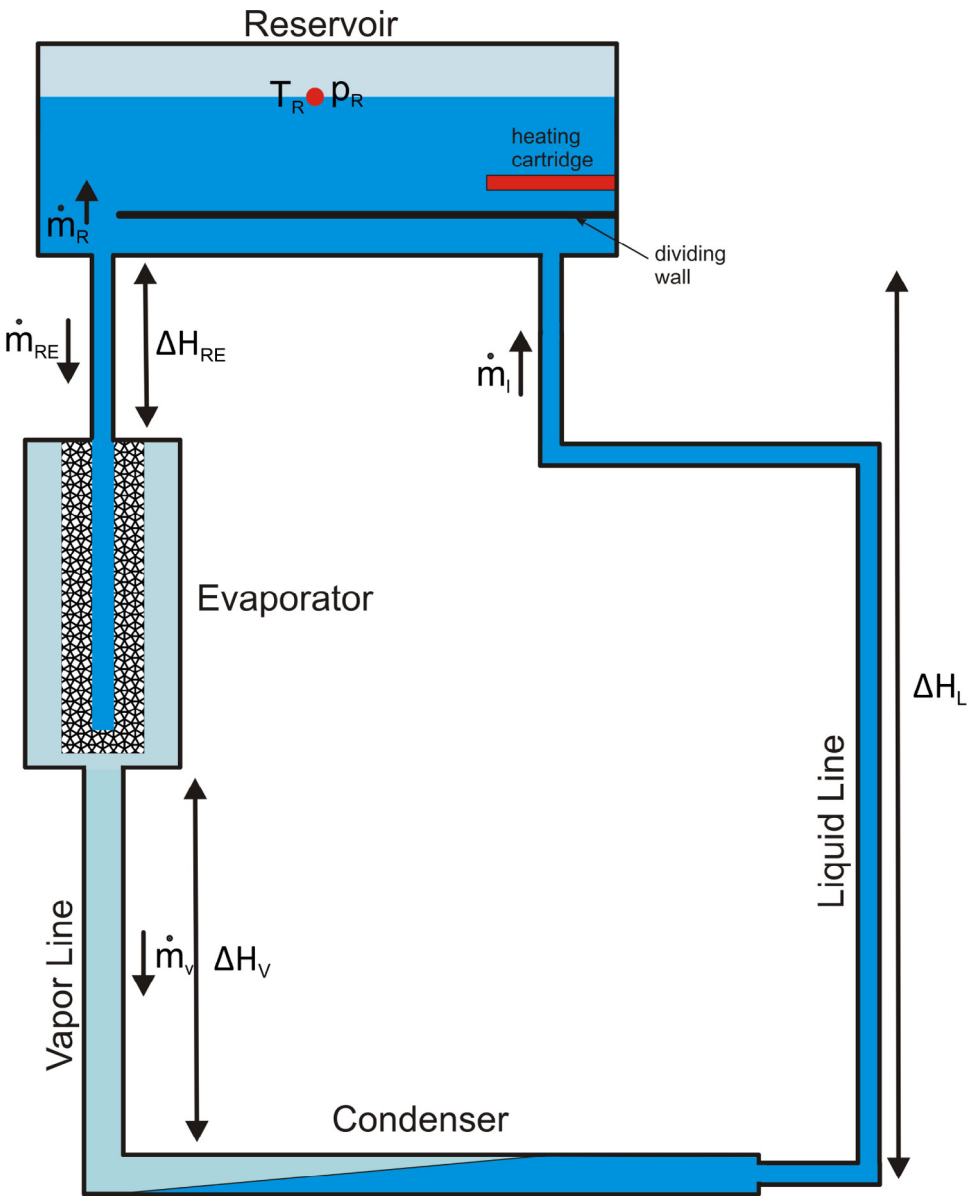

Fig. 1. CPL design.

$$h_m A_C \frac{d\eta}{dt} = \dot{m}_v h_v - \dot{m}_C h_\ell - \phi_C \tag{9}$$

where $\rho_m = (1-\alpha_C)\rho_\ell + \alpha_C \rho_v$ is the average density of the fluid, $h_m = (1-\alpha_C)\rho_\ell h_\ell + \alpha_c \rho_v h_v$ is the average enthalpy of the fluid, h_v and h_ℓ are the mean specific enthalpies of liquid and vapor phases. ϕ_C is the heat flux exchanged with the cold source:

$$\phi_C = \pi D_C \eta K_C (T_C - T_{CS}) \tag{10}$$

where T_{CS} is the cold source temperature and K_C is the heat transfer coefficient which describes the internal exchange between the fluid and the condenser wall, the conduction through the wall and the external thermal exchange between the wall and the cold source.

– Liquid zone

The subcooled liquid zone is characterized by a variable length $L-\eta$. The mass and momentum balances can be expressed by:

$$-\rho_\ell A_C \frac{d\eta}{dt} = \dot{m}_C - \dot{m}_\ell \tag{11}$$

Table 1
CPL dimensions.

Component	Feature	Dimension	Value
Reservoir	Cylindrical	Diameter(mm)	99.6 – 101.6
		Length (mm)	308
	Lower part	Height (mm)	6
		Volume (cm^3)	58.7
Evaporator	Housing	Size (mm^3)	320×81×20
		Thickness (mm)	1
	Porous wick	Size (mm^3)	283×68×16
		Pores (μm)	6.8
		Porosity (%)	73
		Permeability (m^2)	6.5310^{-13}
	Vapor grooves	Trapezoid section (mm)	0.6 – 0.6 – 1.2
		Pitch (mm)	1.8
Condenser	Coaxial	Length (m)	4.04
		Primary diameter (mm)	12–14
		Secondary diameter (mm)	17.3–21.3
Vapor line		Length (m)	1.82
		Diameter (mm)	12–14
Liquid line		Length (m)	1.48
		Diameter (mm)	6–8

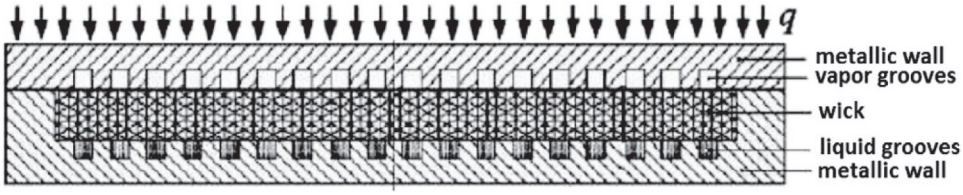

Fig. 2. Schematic of miniature flat plate CPL evaporator [21].

$$\left(\frac{L_C-\eta}{A_C}\right)\frac{d\dot{m}_\ell}{dt}=p_C-p_{L,in}-\Delta p_{C,\ell} \tag{12}$$

where $p_{L,in}$ is the pressure at the liquid line inlet (condenser outlet) and $\Delta p_{C,\ell}$ are the viscous pressure losses in this region, evaluated using Darcy–Weisbach correlation.

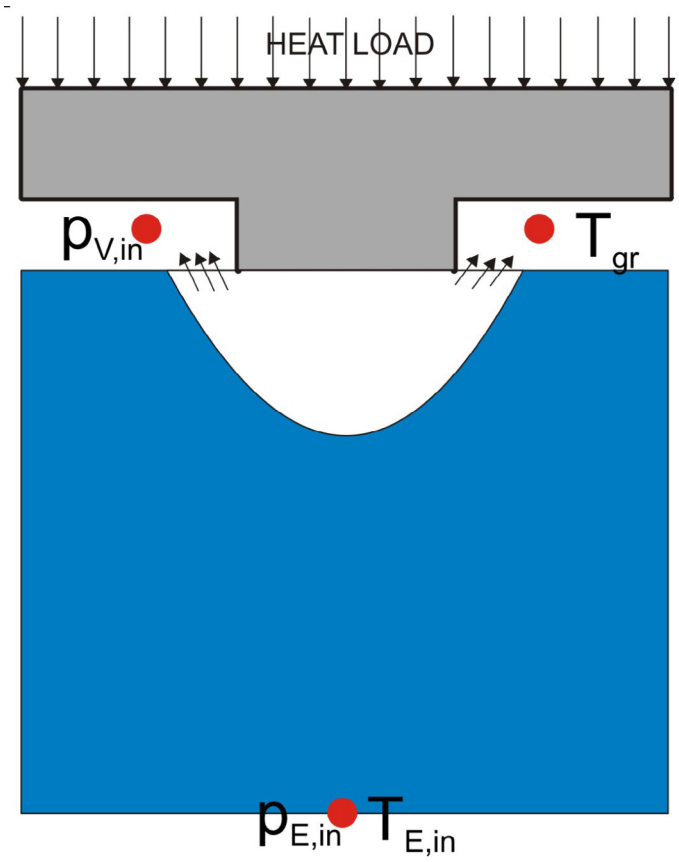

Fig. 3. Unit cell of capillary evaporator internal structure.

According to the experimental results of Kaled et al. [29], the liquid temperature at the condenser outlet is assumed to be constant and equal to the temperature of the cold source:

$$T_{C,o}=T_{CS} \tag{13}$$

2.4. Reservoir

The CPL reservoir is divided into two zones: the liquid lower part and two-phase higher part (Fig. 5). The upper part is filled with both liquid and vapor phases at saturation state during the whole loop operation. The temperature of the higher part of the reservoir is maintained at a fixed value, thanks to a PID regulator. The lower part is filled with liquid. It ensures the liquid supply to the evaporator.

– lower part
The mass balance of the lower part is written as follows:

$$\dot{m}_\ell=\dot{m}_{RE}+\dot{m}_R \tag{14}$$

The liquid temperature in the lower part is calculated, thanks to the energy conservation equation:

$$\rho_\ell\Omega_{R_b}c_{p_\ell}\frac{dT_{R_b}}{dt}=\dot{m}_\ell c_{p_\ell}T_{LR}-\dot{m}_{RE}c_{p_\ell}T_{R_b}-\dot{m}_R c_{p_\ell}T_{R_{bh}}+G_R(T_R-T_{R_b})+h_{R_b,int}S_{R_b,int}(T_{R_bW}-T_{R_b}) \tag{15}$$

$h_{R_b,int}$ is a heat transfer coefficient that describes the internal heat exchanges between the liquid and the reservoir wall; G_R is an empirical conductance determined experimentally by Lachassagne et al. [5], which describes the thermal exchange between the two parts of the reservoir.
The reservoir wall temperature is determined by the following equation:

$$\rho_W\Omega_{R_W}c_{pW}\frac{dT_{R_bW}}{dt}=h_{R_b,ext}S_{R_b,ext}(T_a-T_{R_bW})+h_{R_b,int}S_{R_b,int}(T_{R_b}-T_{R_bW}) \tag{16}$$

$h_{R,ext}$ is a heat transfer coefficient that describes the external heat exchanges.

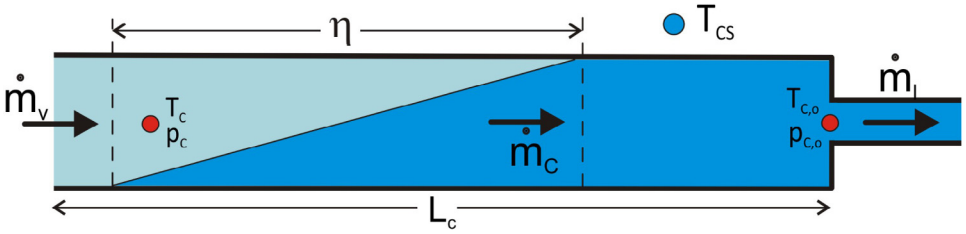

Fig. 4. Condenser section.

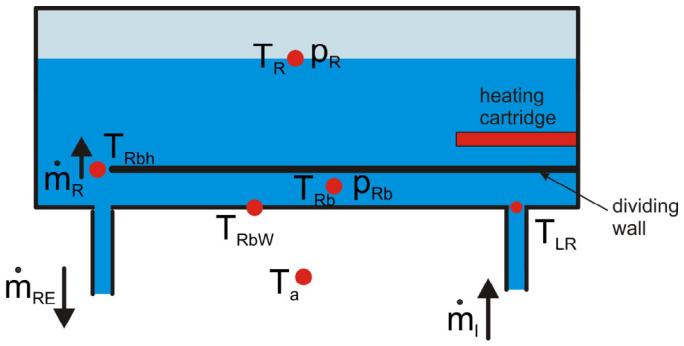

Fig. 5. Reservoir section.

– higher part
According to the experimental results of Kaled et al. [29] and Lachassagne et al. [2], the temperature in the high part of the reservoir is not influenced by the rest of the loop. Its value is fixed by a PID controller. For this reason, the temperature is assumed to be constant.

$$T_R = cste \tag{17}$$

$$p_R = p_{sat}(T_R) \tag{18}$$

2.5. Vapor line

The vapor flow is considered to be incompressible and isothermal [4,5,27,28,30]. The momentum balance is applied to determine the vapor pressure at the vapor line inlet.

$$p_{V,in} = p_C + \frac{L_V}{A_V}\frac{\partial \dot{m}_v}{\partial t} - \Delta p_{g,V} + \Delta p_V \tag{19}$$

where $\Delta p_{g,V} = \rho_v g \Delta H_V$ are the hydrostatic pressure losses and Δp_V are the viscous and singular pressure losses.

2.6. Condenser/reservoir liquid line

To determine the liquid and the wall temperatures, the liquid lines are discretized into small elements of volume. The energy balance equation for each element is written as follows:

– Liquid temperature

$$\rho_\ell c_{p_\ell}\left(\frac{\partial T_\ell}{\partial t} + \vec{v}_\ell \cdot \vec{\nabla} T_\ell\right) = \vec{\nabla}\cdot\left(\lambda_\ell \vec{\nabla} T_\ell\right) \tag{20}$$

For the boundary conditions:

$$-\lambda_\ell \vec{\nabla} T_\ell \cdot \vec{n}\big|_{wall,int} = h_{L,int}(T_\ell - T_W) \quad \text{at the internal wall}$$

$$T_\ell = \begin{cases} T_{CS} & \text{at the condenser outlet if } \dot{m}_\ell > 0 \\ T_{R_b} & \text{at the reservoir inlet if } \dot{m}_\ell < 0 \end{cases}$$

– Wall temperature

$$\rho_W c_{pW}\frac{\partial T_W}{\partial t} = \vec{\nabla}\cdot\left(\lambda_W \vec{\nabla} T_W\right) \tag{21}$$

For the boundary conditions:

$$-\lambda_W \vec{\nabla} T_W \cdot \vec{n}\big|_{wall,int} = h_{L,int}(T_W - T_\ell) \quad \text{at the internal wall}$$

$$-\lambda_W \vec{\nabla} T_W \cdot \vec{n}\big|_{wall,ext} = h_{L,ext}(T_W - T_a) \quad \text{at the external wall}$$

$$T_W = \begin{cases} T_{CS} & \text{at the condenser outlet} \\ T_{RbW} & \text{at the reservoir inlet} \end{cases}$$

where T_ℓ is the liquid temperature, T_W is the wall temperature, $\vec{v}_\ell$ is the liquid velocity, $h_{L,int}$ is a heat transfer coefficient that describes the internal heat exchanges between the liquid and the wall and $h_{L,ext}$ is a heat transfer coefficient that describes the external heat exchanges.

The momentum balance is written as follows:

$$p_{L,in} = p_{L,o} + \frac{L_L}{A_L}\frac{d\dot{m}_\ell}{dt} + \Delta p_L + \Delta p_{g,L} \tag{22}$$

where $p_{L,in}$ and $p_{L,o}$ s are respectively the pressures at the inlet and outlet of the liquid line, $\Delta p_{g,L} = \rho_\ell g \Delta H_L$ are the hydrostatic pressure losses and Δp_L are the viscous and singular pressure losses.

2.7. Reservoir/evaporator liquid line

The liquid is incompressible; the mass flow rate $\dot{m}_{RE}$ is constant (Fig. 5).

The liquid pressure at the porous wick inlet is calculated by the following equation:

$$p_{E,in} = p_{R_b} + \rho_\ell L_{RE}\frac{\partial v_\ell}{\partial t} + \Delta p_{g,RE} - \Delta p_{RE} \tag{23}$$

where $\Delta p_{g,RE} = \rho_\ell g \Delta H_{RE}$ are the hydrostatic pressure losses and Δp_{RE} are the viscous and singular pressure losses.

The liquid line is not adiabatic; the thermal exchange with the external ambiance is taken into account. The liquid and wall temperatures are determined by the following equations:

– Liquid temperature

$$\rho_\ell c_{p_\ell}\left(\frac{\partial T_\ell}{\partial t} + \vec{v}_\ell \cdot \vec{\nabla} T_\ell\right) = \vec{\nabla}\cdot\left(\lambda_\ell \vec{\nabla} T_\ell\right) \tag{24}$$

where $\vec{v}_\ell$ is the liquid velocity.
For the boundary conditions:

$$-\lambda_\ell \vec{\nabla} T_\ell \cdot \vec{n}\big|_{wall,int} = h_{L,int}(T_\ell - T_W) \quad \text{at the internal wall}$$

$$T_\ell = T_{R_b} \quad \text{at the reservoir outlet}$$

– Wall temperature

$$\rho_W c_{pW}\frac{\partial T_W}{\partial t} = \vec{\nabla}\cdot\left(\lambda_W \vec{\nabla}_W\right) \tag{25}$$

For the boundary conditions:

$$-\lambda_W \vec{\nabla} T_W \cdot \vec{n}\big|_{wall,int} = h_{L,int}(T_W - T_\ell) \quad \text{at the internal wall}$$

$$-\lambda_W \vec{\nabla} T_W \cdot \vec{n}\big|_{wall,ext} = h_{L,ext}(T_W - T_a) \quad \text{at the external wall}$$

$$T_W = \begin{cases} T_C & \text{at the extremity which is in contact with evaporator casing} \\ T_{R_{bW}} & \text{at the extremity which is in contact with reservoir wall} \end{cases}$$

2.8. Liquid at the inlet evaporator

The cross-section in Fig. 6 shows that the liquid delivered by the reservoir feeds the porous wick through three liquid arteries. In this model, we consider the influence of the parasitic heat flux on the liquid temperature at the porous wick inlet.

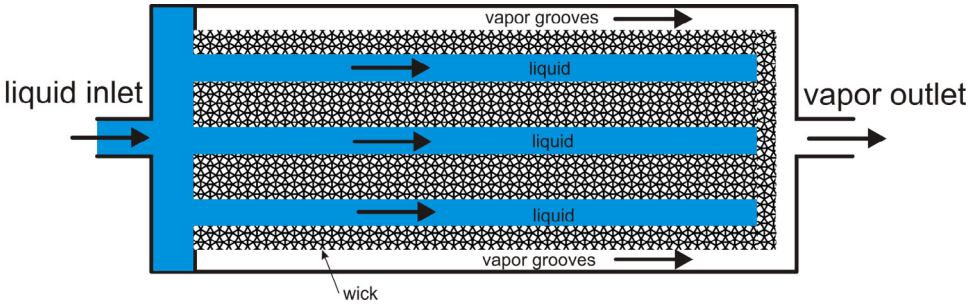

Fig. 6. Evaporator section [5].

The energy balance can be written as follows:

$$\rho_\ell c_{p_\ell} \Omega_{E,in} \frac{dT_{w,in}}{dt} = \dot{m}_{RE} c_{p_\ell} (T_{RE,o} - T_{w,in}) + \phi_p \quad (26)$$

where $T_{RE,o}$ is the liquid temperature at the reservoir/evaporator liquid line outlet, ϕ_p is the parasitic heat flux calculated at the porous wick inlet and $\Omega_{E,in}$ is the liquid volume at the evaporator inlet before entering the porous wick.

3. Results and discussion

An experimental test bench has been developed at Alstom Transport with evaporator/reservoir assembly designed by Euro Heat Pipes company to cool high dissipative power electronics in a railroad traction chain. The mathematical model was validated in transient regime by comparing the simulations results to experimental data of a methanol CPL [14]. It can be shown from Fig. 7 that a good agreement between these data was observed. The maximum difference between the predicted and measured temperatures does not exceed 1 °C.

3.1. Results in steady-state conditions: effect of working fluid

The working fluids, which are acetone, methanol and ethanol, are considered the most common working fluids among gravitational CPL applications. The thermo-physical properties of these fluids are listed in Table 2.

Fig. 8 shows the Pressure–Temperature diagram for the three working fluids for the same operating conditions ($Q = 3000$ W, $T_R = 80$ °C, $T_{CS} = 40$ °C). It describes the operation process of the CPL, which will be detailed in the following sections.

Fig. 9 presents the evolution of the vapor mass flow rate at the outlet of the evaporator for different working fluids, as a function of the applied power. For each fluid, the vapor mass flow rate increases logically with the input power. It is observed that the vapor mass flow rate increases sequentially from methanol to ethanol and acetone as it is inversely proportional to the heat latent of vaporization ($L_{v,met} > L_{v,eth} > L_{v,ace}$).

Fig. 10 shows the evolution of the vaporized heat flux ($\dot{m}_v L_v$) and the parasitic heat flux for the three working fluids, at a steady state. For the vaporized heat flux, the trends of all the working fluids are

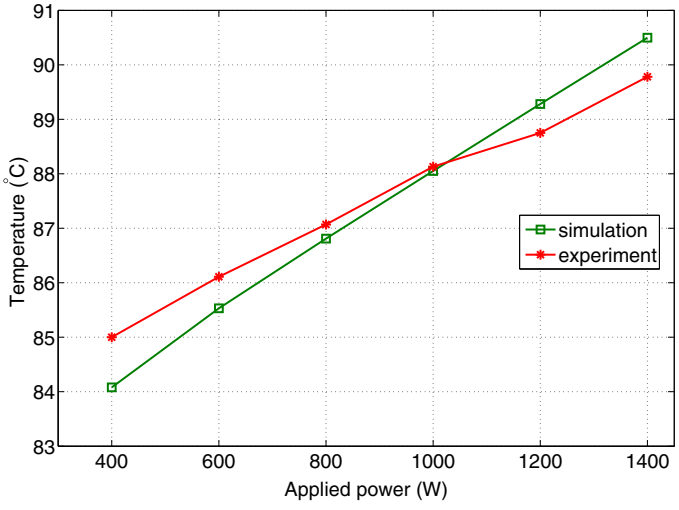

Fig. 7. Comparison of the casing temperature between experiment and simulation.

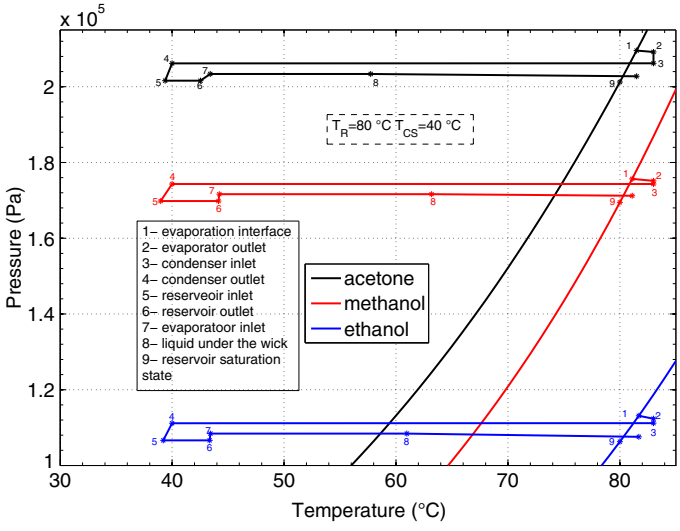

Fig. 8. Pressure/temperature diagram of the CPL operation.

Table 2
Thermo-physical properties of the working fluids at 80 °C.

Working fluid	Liquid density kg/m^3	Latent heat kJ/kg	Liquid specific heat $kJ/(kgK)$	Thermal conductivity $W/(mK)$	Dynamic viscosity $W/(kg.K)$
Methanol	731.97	1065	2.9640	0.1845	2.99910^{-4}
Ethanol	731.94	837.2	3.029	0.1536	4.27910^{-4}
Acetone	719.0172	485.55	2.39	0.137	1.98810^{-4}

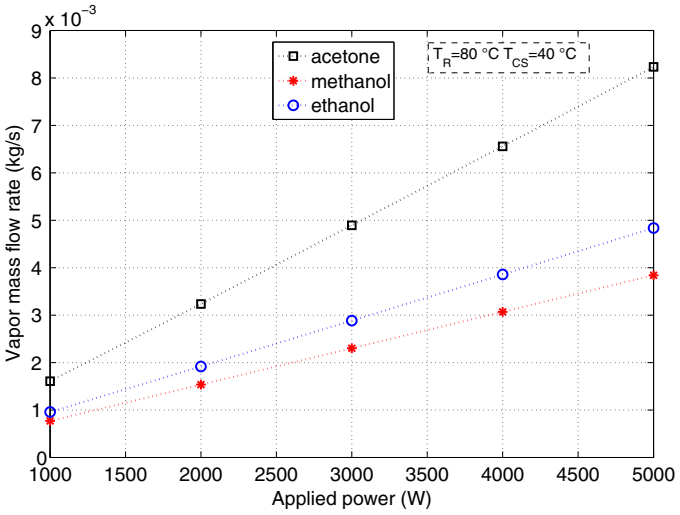

Fig. 9. Vapor mass flow rate.

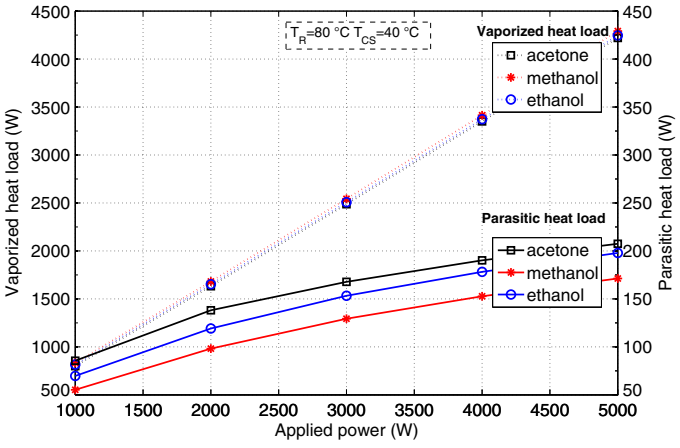

Fig. 10. Heat transfer in the CPL evaporator.

almost the same; therefore it can be deduced that the phase change transfers the same heat load regardless of the used working fluid. The parasitic heat flux is the heat flux loss by conduction across the porous wick inlet. It essentially depends on the effective thermal conductivity and the liquid subcooling at the porous wick inlet. Although methanol has the highest thermal conductivity among the three working fluids, its parasitic heat flux is the lowest. In fact, the effective thermal conductivity does not change greatly from one fluid to another (for a saturated porous wick, the variation of λ_{eff} for the three fluids is less than 3.5% with respect to acetone). However, methanol has the lowest subcooling at the porous wick inlet as shown in Fig. 13. Therefore, it can be deduced that the parasitic heat flux evolution is governed by the subcooling at the porous wick. For all working fluids, the vaporized heat flux and the parasitic heat flux represent approximately 88.5% of the applied power. The rest corresponds to the heat flux exchanged between the evaporator body and the vapor contained in the grooves and the sensible heat flux given to the liquid and the vapor in the wick.

Fig. 11 illustrates the evolution of the liquid temperature at the reservoir inlet for different working fluids as a function of the applied power. The temperature of liquid decreases during its passage from the condenser to the reservoir, due to the exchange with the atmosphere. At steady state, the liquid must be displaced at a mass flow rate equal to the mass flow rate of the vapor leaving the evaporator. An increase in applied power causes an increase in liquid mass flow rate and reduces the time of fluid flow inside the liquid

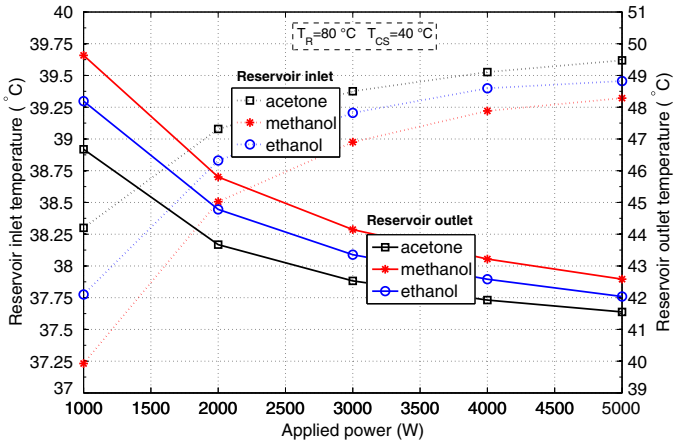

Fig. 11. Liquid temperature at the reservoir inlet and the reservoir outlet.

line. Acetone, with the highest liquid mass flow rate, enters the reservoir with the highest temperature. It is also observed that the difference between the temperatures of the three working fluids decreases as the applied power increases.

Fig. 11 also depicts the liquid temperature at the reservoir outlet for different working fluids. Since the reservoir temperature at the upper part T_R (equal to 80 °C) is greater than that of the liquid entering the reservoir, liquid flowing through the lower part of reservoir is then heated, due to heat transfer between the two reservoir parts. Due to its rapid inflow inside the reservoir, acetone has the lowest temperature at the reservoir outlet. This figure also demonstrates that by increasing the heat load, the liquid temperature at the reservoir outlet decreases for all working fluids.

The liquid at the evaporator inlet is sensitive to the liquid line wall temperature due to heat conduction from the evaporator body. It is also dependent on the liquid flow inside the reservoir/evaporator liquid line. Fig. 12 shows the evolution of liquid temperature at the evaporator inlet for different types of working fluid. At low heat load, it is found that methanol is the hottest working fluid and acetone is the coldest, which is in agreement with the order of the liquid temperature at the reservoir outlet. When the heat load becomes more important, the liquid temperature for acetone decreases slightly compared to methanol and ethanol (acetone reaches ethanol temperature at 3000 W and methanol temperature at 5000 W). Indeed, the acetone flow becomes turbulent inside the liquid line ($Re_l = 2610.65$ for a heat load of 3000 W), which significantly increases the thermal exchange with the hot wall, while the flow of ethanol and methanol is still laminar.

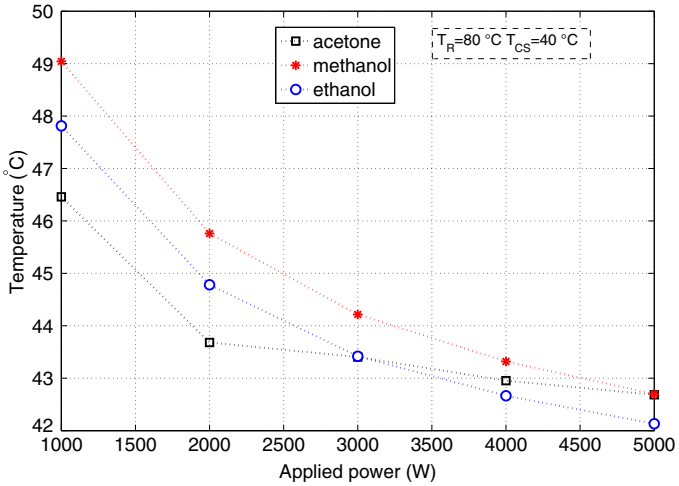

Fig. 12. Liquid temperature at the evaporator inlet.

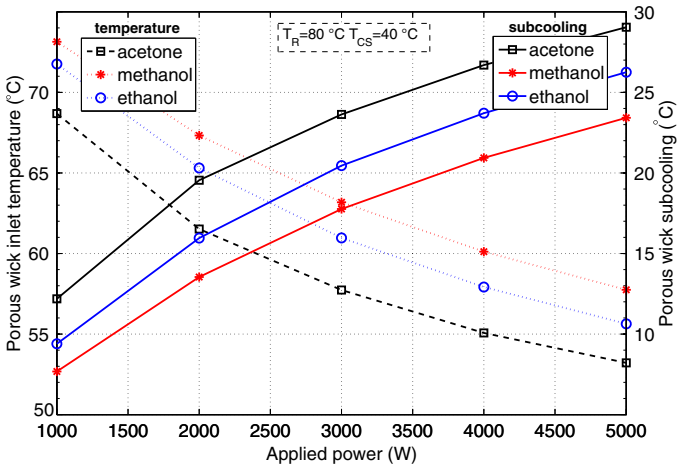

Fig. 13. Liquid temperature and subcooling at the porous wick inlet.

At steady state, the liquid temperature at the porous wick inlet is determined by the following equation:

$$T_{w,in} = T_{RE,o} + \frac{\phi_p}{\dot{m}_v c_{p_\ell}} \tag{27}$$

This equation shows the important role of the parasitic heat flux. The liquid temperature at the porous wick inlet also depends on the heat capacity of the liquid, its mass flow rate and its temperature at the evaporator inlet. Fig. 13 shows the evolution of the liquid temperature at the inlet of the porous wick, for the three fluids. Although, acetone has the largest parasitic heat flux (Fig. 10) and its temperature at the evaporator inlet is higher than that of ethanol for high heat load (Fig. 12), its temperature is always the lowest at the inlet of the porous wick; this behavior is explained by the importance of the mass flow rate of acetone compared to the two other fluids. Stable operation of the CPL requires a sufficient subcooling at the porous wick inlet to prevent deprime. Fig. 13 also shows the subcooling, calculated as the difference between the saturation temperature and the liquid temperature at the porous wick inlet, for different working fluids. It can be seen that the subcooling increases with applied power. Methanol has always the lowest subcooling compared to other fluids.

Fig. 14 demonstrates that the casing temperature varies significantly with the used working fluid. For acetone, the casing temperature profile is very close to that of ethanol. As can be seen, lower casing temperatures are obtained for methanol in comparison with acetone and ethanol, thus methanol has the highest thermal performance. The differences between the working fluids increase with the increasing of applied power. For a heat load of 5 kW, the casing temperature difference between methanol and other working fluids is more than 5 °C. The highest thermal performance of methanol can be explained by the fact that it has the smallest vapor pocket developed inside the porous wick (Fig. 17).

The CPL performance is generally described by the thermal conductance, which is calculated by the following equation:

$$G = \frac{Q}{T_{C_E} - T_R} \tag{28}$$

where T_{C_E} is the casing temperature and T_R is the reservoir temperature.

The thermal behavior difference between the working fluids is also found at the level of the overall conductance of the CPL. It can be seen from Fig. 15 that the CPL conductance is much more important for methanol than for ethanol and acetone. The thermal performance of the last two fluids still close over the entire power range. Nevertheless, one can see that acetone is a bit more efficient than ethanol at low power, while the situation is reverse at high power.

Fig. 16 shows the evolution of the pressure drop across the evaporator as a function of the applied power. It is a combination of

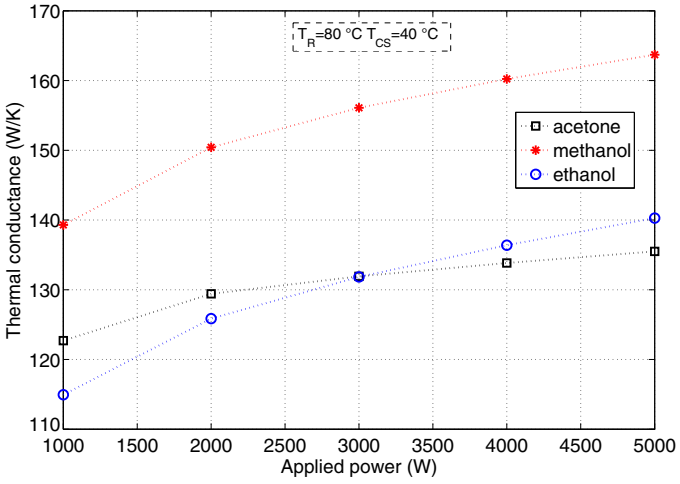

Fig. 15. CPL conductance.

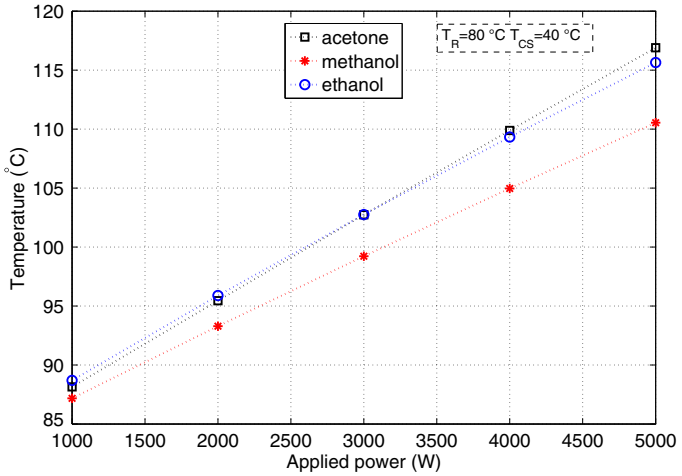

Fig. 14. Casing temperature.

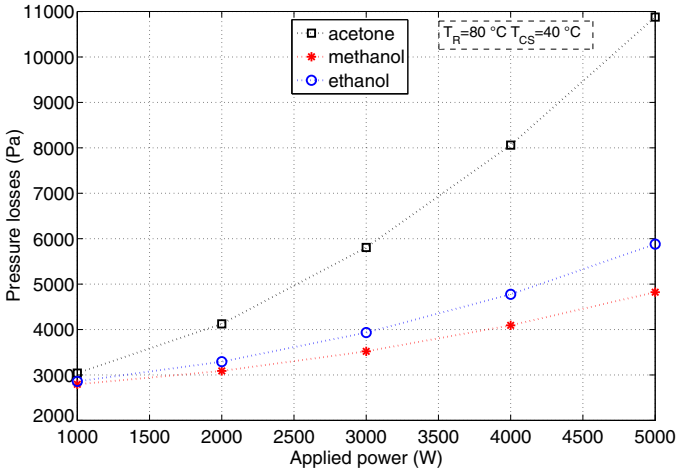

Fig. 16. Pressure difference in the loop.

DOI : 10.1016/j.applthermaleng.2016.02.034

gravity pressure drop and viscous pressure losses in the vapor line, condenser and liquid lines. The change in pressure drop follows obviously that of the mass flow rate. We have seen that methanol is the most efficient fluid in terms of thermal performance. It is also the most interesting fluid in terms of the heat transport capacity of the CPL. The maximum capillary pressure jump is reached for a power of 5 kW for acetone, while it is reached for a power of 10.3 kW for methanol.

The size of the vapor pocket inside the wick depends on several parameters, the most important being the thermophysical properties of the fluid, the saturation temperature and the liquid subcooling at the inlet of the evaporator. Fig. 17 shows, for the three fluids, the vapor pocket developed within the porous wick for a power of 2 kW. It can be seen that their dimensions are relatively close. Nevertheless, the use of methanol leads to the smallest vapor pocket, although it has the lowest subcooling at the porous wick inlet. The vapor pockets of acetone and ethanol are very similar, although the latent heat of acetone is significantly lower than that of ethanol. This can be explained by the fact that ethanol has a lower saturation temperature than acetone (its pressure losses are smaller) and the subcooling at the wick inlet is lower than acetone.

3.2. *Results in transient conditions: study of start-up conditions*

The start-up process consists of heating the evaporator to reservoir temperature and clearing of liquid from the vapor line until the vapor front is established inside the condenser [31–33]. The time required to initiate boiling inside the evaporator depends upon the

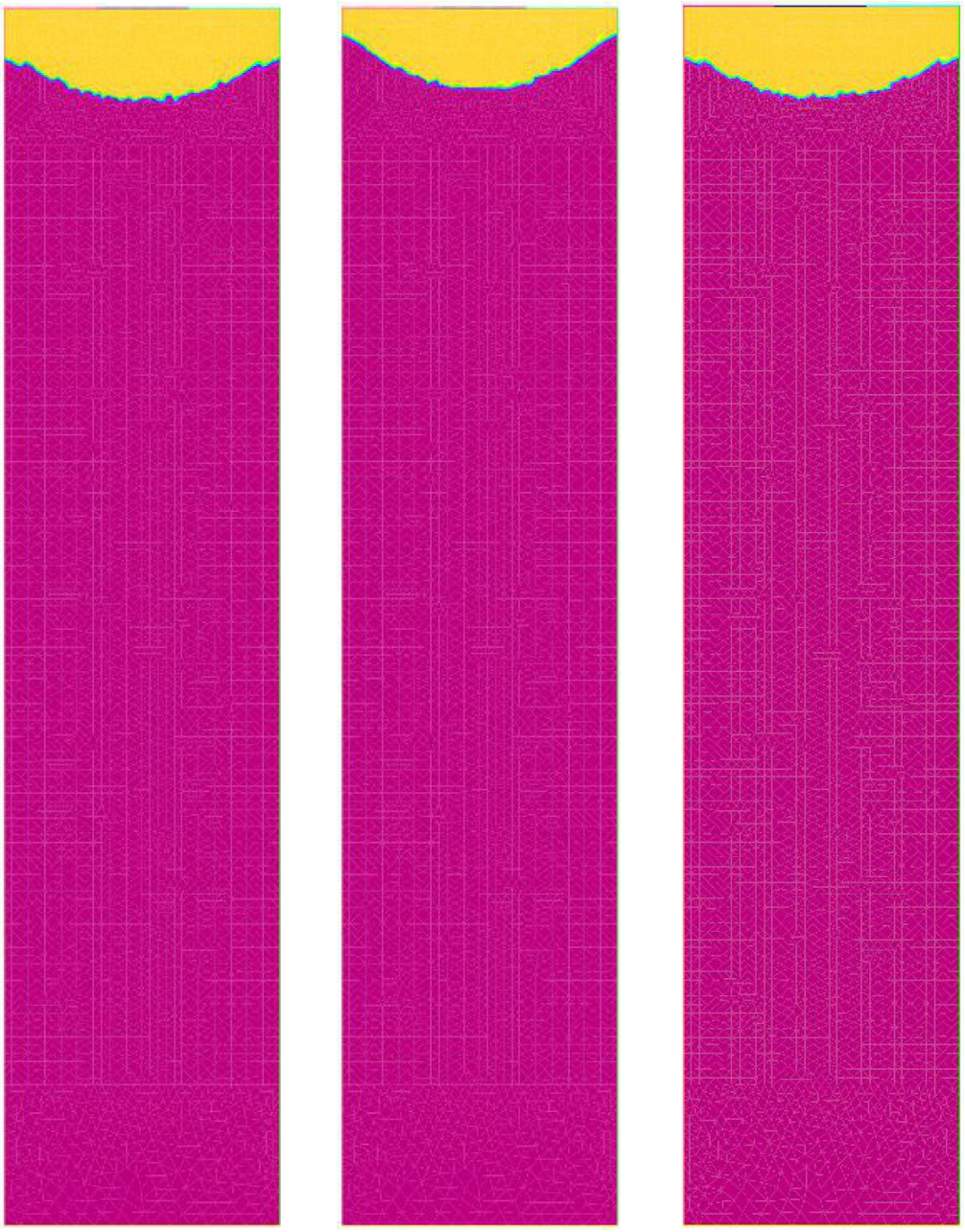

Fig. 17. Vapor pocket for different working fluids.

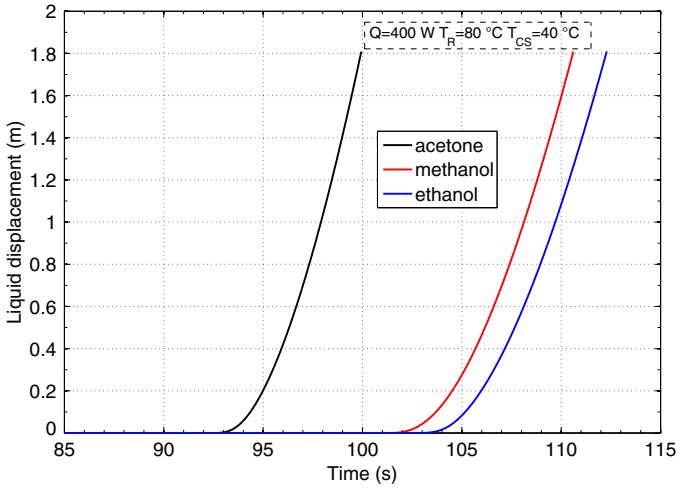

Fig. 18. Liquid displacement inside the vapor line for a heat load of 400 W.

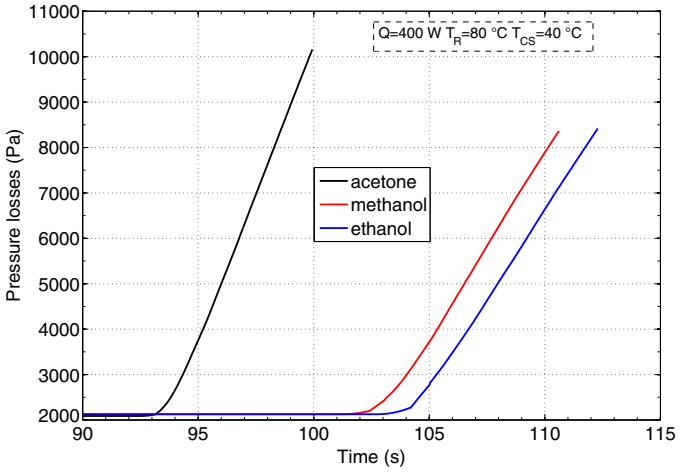

Fig. 19. Pressure losses at the CPL start up for a heat load of 400 W.

heat load, the initial state of the fluid in the evaporator, the working fluid properties and the superheat caused by the presence of nucleation sites inside the porous wick. The modeling of the CPL start-up is based on the following assumptions:

- The time required for initial conditioning of the reservoir is not included in our model: at the start-up, the reservoir temperature is already set at 80 °C;
- Initially, the grooves are assumed to be filled with vapor: the time required for the clearing of the vapor grooves during start-up is not taken into account;
- The presence of nucleation sites is not included in our model. However, Lossouarn [34] demonstrates experimentally that the presence of these sites causes an overheating of 10 °C, which could delay the start-up.

The displacement of the vapor front in the vapor line is described by the following equation:

$$\frac{\partial \beta}{\partial t} = \frac{\dot{m}_v}{\rho_v A_v} \tag{29}$$

Fig. 18 shows the evolution of the position of liquid/vapor interface inside the vapor line for a heat load of 400 W. It can be seen that acetone has the lowest time required to initiate boiling inside the evaporator compared to other fluids. In fact, the temperature of acetone inside the porous wick rises rapidly due to low liquid specific heat. Acetone presents also the smallest time required (7.48 s) to clear the vapor line from liquid.

During the CPL start-up, the liquid is pushed through the vapor line at a velocity equal to the velocity of the vapor leaving the evaporator. The relation between the liquid and vapor mass flow rates is described by the following equation:

$$\dot{m}_\ell = \frac{\rho_\ell}{\rho_v}\dot{m}_v \tag{30}$$

Fig. 19 describes the evolution of the pressure drop across the evaporator as a function of time for different working fluids. The higher liquid mass flow rate at CPL start-up imposes a large pressure drop called pressure surge [31]. For all working fluids, the pressure drop across the evaporator increases with time and the viscous pressure losses in the liquid line are the most important. As for the steady-state pressure drop shown in Fig. 16, methanol, at the CPL start-up, presents the lowest pressure losses.

3.3. *Effect of the wick properties*

The objective of this section is to investigate the effect of the porous wick properties on the performance of Capillary Pumped Loop. We only emphasize the effect of the thermal conductivity and the porosity on the CPL operation.

As mentioned above, the determination of the effective thermal conductivity of the porous wick is difficult to evaluate accurately. Fig. 20 shows the casing temperature for different models found in the literature, for a heat load of 1000 W. The casing temperature varies significantly from parallel model to series model. In the lack of experimental data, the effective thermal conductivity is evaluated by a parallel model, which is the common used model.

Fig. 21 describes the evolution of the depth of the vapor pocket inside the porous wick as a function of the solid thermal conductivity for a capillary pumped loop filled with methanol for a heat load of 2 kW. A high value of thermal conductivity causes an important parasitic heat flux, which results in an increase in the liquid temperature at the porous wick inlet. Accordingly, liquid inside the porous wick requires less energy to reach the saturation temperature. This may explain the increase in the vapor pocket depth.

Fig. 22 plots the casing temperature as a function of time for different solid thermal conductivities. It is observed that the casing

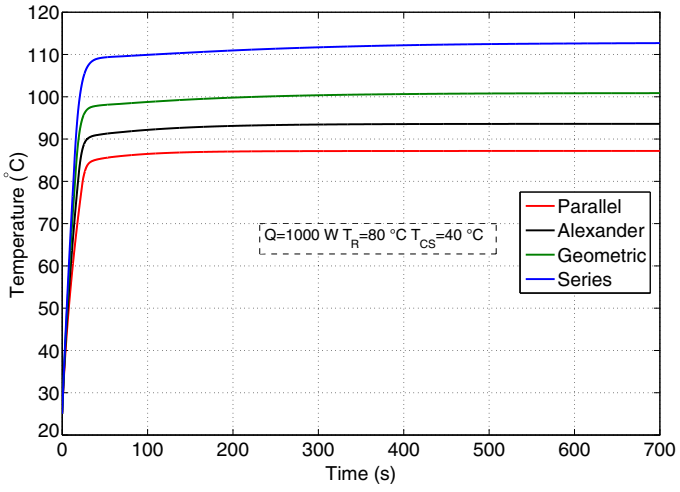

Fig. 20. Casing temperature profiles for different models of effective thermal conductivity.

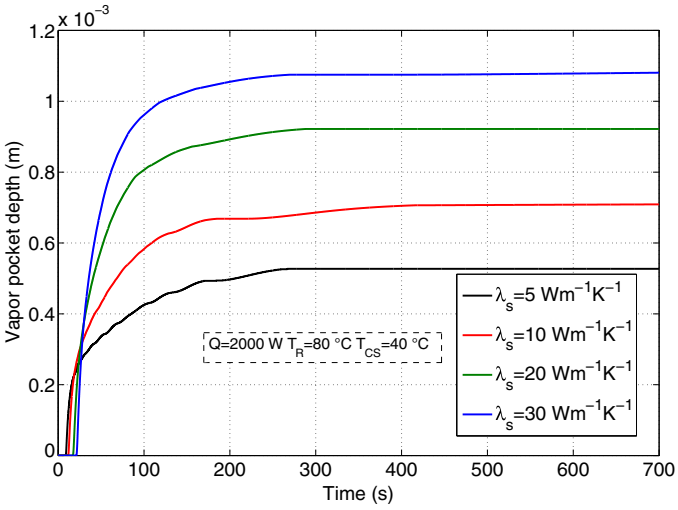

Fig. 21. Effect of the thermal conductivity on the vapor pocket depth.

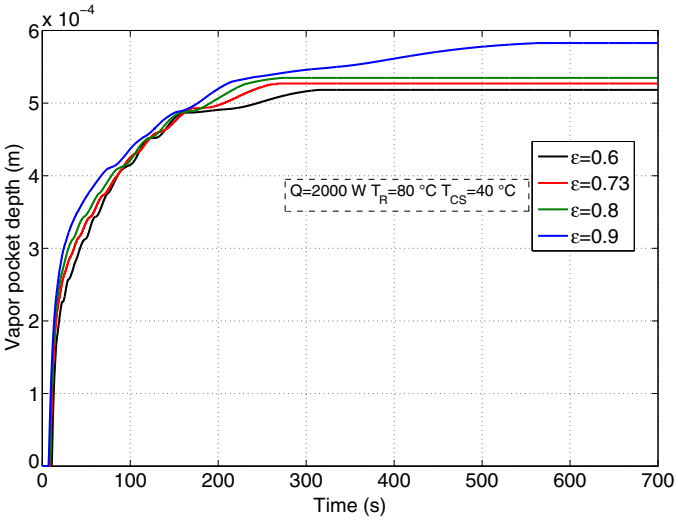

Fig. 23. Effect of the porosity on the vapor pocket depth.

temperature decreases by increasing the thermal conductivity because the high thermal conductivity helps to transfer heat efficiently to the evaporating menisci in the capillary structure by conduction.

The obtained results are in accordance with the numerical study of Coquard [12]. Low conductivities greatly reduce the risk of percolation. However, it causes a high casing temperature that is in contact with the electronic components. Therefore, using a porous wick with several layers of different thermal conductivities will be a better solution to improve the CPL performance.

The porosity of the wick affects the parasitic heat flux from the casing to the wick inlet as the effective thermal conductivity of the wick structure has strong dependence on the porosity ($\lambda_{eff,l}=(1-\varepsilon)\lambda_s+\varepsilon\lambda_l$, $\lambda_{eff,v}=(1-\varepsilon)\lambda_s+\varepsilon\lambda_v$). Fig. 23 illustrates the vapor pocket depth for different porosities. It can be shown that the lower porosity reduces the vapor pocket inside the porous wick.

Fig. 24 presents the effect of porosity on the casing temperature. When the porosity increases, the effective thermal conductivity decreases. As a result, the casing temperature increases. It should then avoid using wick with high porosity.

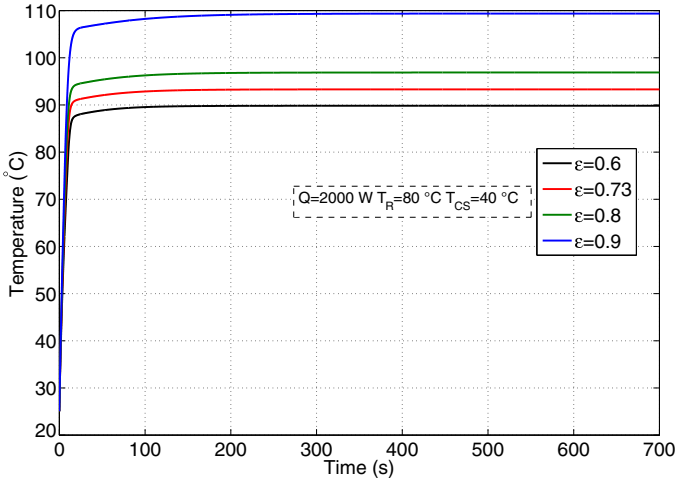

Fig. 24. Effect of the porosity on the casing temperature.

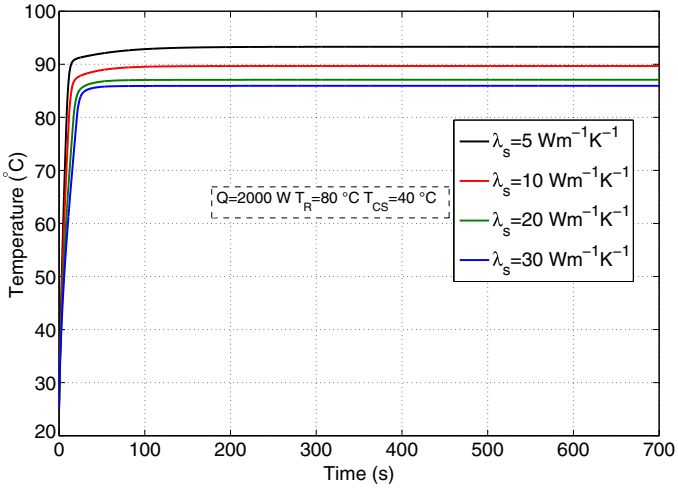

Fig. 22. Effect of the thermal conductivity on the casing temperature.

4. Conclusion

In the study, a transient overall model has been developed to predict the thermal and hydrodynamic behavior of a capillary pumped loop. The originality of the proposed model consists of the precise description of the heat and mass transfer inside the porous wick. The model has been confronted to a set of experimental data. A good agreement is found between experimental and theoretical results for the entire heat input range. The operational characteristics of CPL with different working fluids and porous wick properties are analyzed and several conclusions can be summarized as follows:

- The CPL methanol has the lower evaporator wall temperature.
- From the point of view of thermal conductance, methanol is the most efficient fluid at the same operation condition.
- At the same operation condition, methanol has the highest heat transport capacity.
- Evaporator with low conductivity can reduce the risk of an eventual evaporator deprime, but it causes a high casing temperature.
- Evaporator with large porosity can increase the risk of percolation and causes a high casing temperature.

In the future, many efforts should be dedicated to the modeling of the phase change phenomena inside the condenser. The fluid compressibility effects inside the condenser and the vapor line should be also taken into account to improve the description of the thermal and hydraulic phenomena occurring in the whole loop.

Acknowledgement

The work presented in this paper is supported by Alstom Transport, site de Tarbes (Contract Number 11099).

Nomenclature

a	Accommodation number [ambient]
R	Universal gas constant [$Jmol^{-1}K^{-1}$]
M	Molar mass of fluid [$kg\ mol^{-1}$]
C_p	Specific heat [$Jkg^{-1}K^{-1}$]
K	Heat transfer coefficient [$Wm^{-2}K^{-1}$]
h	Convective heat transfer coefficient [$Wm^{-2}K^{-1}$]
h	Specific enthalpy [Jkg^{-1}]
A	Surface [m^2]
A	Cross section [m^2]
D	Diameter [m]
L	Length [m]
G	Thermal conductance [WK^{-1}]
Q	Input power [W]
Re	Reynolds number
L_v	Latent heat of vaporization [$J\ kg^{-1}$]
p	Pressure [Pa]
t	Time [s]
T	Temperature [K]
V	Darcian velocity [$m\ s^{-1}$]
v	Velocity [$m\ s^{-1}$]
g	Gravitational acceleration [$m\ s^{-2}$]

Greek symbols

α	Volumetric fraction
β	Vapor front position [m]
κ	Permeability [m^2]
κ_r	Relative permeability
λ	Thermal conductivity [$Wm^{-1}K^{-1}$]
μ	Dynamic viscosity [$kg\ m^{-1}s^{-1}$]
η	Two-phase zone length [m]
ρ	Density [$kg\ m^{-3}$]
ϕ	Heat flux [W]
$\dot{\Gamma}$	Volumetric mass rate of phase change [$kg\ m^{-3}s^{-1}$]
$\dot{m}$	Mass flow rate [$kg\ s^{-1}$]
Ω	Volume [m^3]

Subscripts

ℓ	Liquid
v	Vapor
s	Solid
eff	Effective
cap	Capillary
sat	Saturation
gr	Groove
R	Reservoir
E	Evaporator
C	Condenser
C_E	Casing
V	Vapor line
L	Liquid line
b	Bottom part
h	High part
CS	Cold source
in	Inlet
o	Outlet
W	Wall
w	Wick
int	Internal
ext	External
p	Parasitic

References

[1] F.J. Stenger, Experimental feasibility study of water-filled capillary-pumped heat-transfer loop, Lewis Research Center, Ohio (NASA TM X-1310).
[2] L. Lachassagne, V. Ayel, C. Romestant, Y. Bertin, Experimental study of capillary pumped loop for integrated power in gravity field, Appl. Therm. Eng. 35 (2012) 166–176.
[3] V. Dupont, S. Van Oost, L. Barremaecker, Railways qualification tests of capillary pumped loop on a train, in: 17th International Heat Pipe Conference (17th IHPC), Kanpur, India, 2013.
[4] E. Pouzet, J.-L. Joly, V. Platel, J.-Y. Grandpeix, C. Butto, Dynamic response of a capillary pumped loop subjected to various heat load transients, Int. J. Heat Mass Transf. 47 (2003) 2293–2316.
[5] L. Lachassagne, V. Ayel, C. Romestant, Y. Bertin, Steady-state modeling of capillary pumped loop in gravity field, Int. J. Therm. Sci. 64 (2013) 62–80.
[6] N. Delalandre, V. Ayel, J. Salat, Transient Thermohydraulic Modeling of Capillary Pumped Loop, SAE International, 2011.
[7] C. Figus, Y. Le Bray, S. Bories, M. Prat, Heat and mass transfer with phase change in a porous structure partially heated: continuum model and pore network simulations, Int. J. Heat Mass Transf. 42 (1999) 2557–2569.
[8] Z.M. Wan, W. Liu, Z.K. Tu, A. Nakayama, Conjugate numerical analysis of flow and heat transfer with phase change in a miniature flat plate CPL evaporator, Int. J. Heat Mass Transf. 52 (2009) 422–430.
[9] M.A. Chernysheva, Y.F. Maydanik, 3D-model for heat and mass transfer simulation in flat evaporator of copper-water loop heat pipe, Appl. Therm. Eng. 33–34 (2012) 124–134.
[10] T. Kaya, J. Goldak, Numerical analysis of heat and mass transfer in the capillary structure of a loop heat pipe, Int. J. Heat Mass Transf. 49 (17–18) (2006) 3211–3220.
[11] R. Boubaker, V. Platel, A. Berges, M. Bancelin, E. Hannezo, Dynamic model of heat and mass transfer in an unsaturated porous wick of capillary pumped loop, Appl. Therm. Eng. 76 (2015) 1–8.
[12] T. Coquard, Coupled heat and mass transfer in an element of a capillary evaporator (Ph.D. thesis), Institut National Polytechnique de Toulouse, Toulouse, France, 2006 (in French).
[13] L. Mottet, T. Coquard, M. Prat, Three dimensional liquid and vapour distribution in the wick of capillary evaporators, Int. J. Heat Mass Transf. 83 (2015) 636–651.
[14] R. Boubaker, V. Platel, Vapor pocket behavior inside the porous wick of a capillary pumped loop for terrestrial application, Appl. Therm. Eng. 84 (2015) 420–442.
[15] H. Han, X. Cui, Y. Zhu, S. Sun, A comparative study of the behavior of working fluids and their properties on the performance of pulsating heat pipes (PHP), Int. J. Therm. Sci. 82 (2014) 138–147.
[16] E. Bazzo, R. Riehl, Operation characteristics of a small-scale capillary pumped loop, Appl. Therm. Eng. 23 (2003) 687–705.
[17] Z. Liu, D. Gai, H. Li, W. Liu, J. Yang, M. Liu, Investigation of impact of different working fluids on the operational characteristics of miniature LHP with flat evaporator, Appl. Therm. Eng. 31 (2011) 3387–3392.
[18] R. Singh, A. Akbarzadeh, M. Mochizuki, Effect of wick characteristics on the thermal performance of the miniature loop heat pipe, J. Heat Transfer 131 (2009) 82–601.
[19] P.H. Santos, E. Bazzo, S. Becker, R. Kulenovic, R. Mertz, Development of LHPs with ceramic wick, Appl. Therm. Eng. 30 (2010) 1784–1789.
[20] P.H. Santos, E. Bazzo, A. Amir Oliveira, Thermal performance and capillary limit of a ceramic wick applied to LHP and CPL, Appl. Therm. Eng. 41 (2012) 92–103.
[21] Z. Wan, J. Liu, J. Wan, Z. Tu, W. Liu, An overall numerical investigation on heat and mass transfer for miniature flat plate capillary pumped loop evaporator, Thermochim. Acta 518 (1–2) (2011) 82–88.
[22] Y. Cao, A. Faghri, Analytical solutions of flow and heat transfer in a porous structure with partial heating and evaporation on the upper surface, Int. J. Heat Mass Transf. 37 (10) (1994) 1525–1533.
[23] M. Chernysheva, Y. Maydanik, Numerical simulation of transient heat and mass transfer in a cylindrical evaporator of a loop heat pipe, Int. J. Heat Mass Transf. 51 (17–18) (2008) 4204–4215.
[24] Z.C. Liu, W. Liu, A. Nakayama, Flow and heat transfer analysis in porous wick of CPL evaporator based on field synergy principle, Heat Mass Transfer 43 (12) (2007) 1273–1281.
[25] X.M. Huang, W. Liu, A. Nakayama, S.W. Peng, Modeling for heat and mass transfer with phase change in porous wick of CPL evaporator, Heat Mass Transfer 41 (7) (2005) 667–673.
[26] P. Soler, Experimental investigation and thermohydraulic modeling of a Loop Heat Pipe: study of the coupling between the compensation chamber and the evaporator (Ph.D. thesis), Université de Provence, France, 2009 (in French).

[27] S. Launay, V. Platel, S. Dutour, J.-L. Joly, Transient modeling of loop heat pipes for the oscillating behavior study, J. Thermophys. Heat Transfer 21 (3) (2007) 487–495.
[28] S. Launay, V. Sartre, J. Bonjour, Analytical model for characterization of loop heat pipes, J. Thermophys. Heat Transfer 22 (4) (2008) 623–631.
[29] A. Kaled, S. Dutour, V. Platel, J. Lluc, Experimental study of a capillary pumped loop for cooling power electronics: response to high amplitude heat load steps, Appl. Therm. Eng. 89 (2015) 169–179.
[30] B. Siedel, V. Sartre, F. Lefèvre, Complete analytical model of a loop heat pipe with a flat evaporator, Int. J. Therm. Sci. 89 (2015) 372–386.
[31] K.R. Wrenn, Capillary pumped loop performance investigation through flow visualization (Ph.D. thesis), University of Maryland, USA, 2004.
[32] J. Ku, L. Ottenstein, C.D. Butler, T. Swanson, D. Thies, Thermal performance of capillary pumped loops onboard terra spacecraft, in: SAE Technical Paper Series, SAE International, 2004.
[33] Z. Liu, W. Liu, J. Yang, Experimental investigation of new flat-plate-type capillary pumped loop, J. Thermophys. Heat Transfer 22 (1) (2008) 98–104.
[34] D. Lossouarn, Theoretical and experimental study of a capillary pumped loop for cooling power converters with a high heat flux density for the railway traction (Ph.D. thesis), Université de Poitiers, Poitiers, France, 2008 (in French).